Human influence on the 2021 British Columbia floods

Nathan P. Gillett, Alex J. Cannon, Elizaveta Malinina, Markus A. Schnorbus, Faron Anslow, Qiaohong Sun, Megan C. Kirchmeier-Young, Francis W. Zwiers, Christian Seiler, Xuebin Zhang, Greg Flato, Hui Wan, Guilong Li, & Armel Castellan

2022

Pacific Climate Impacts Consortium (PCIC)

PCIC Publications

Original citation:

Gillett, N. P., Cannon, A. J., Malinina, E., Schnorbus, M. A., Anslow, F., Sun, Q., Kirchmeier-Young, M. C., Zwiers, F. W., Seiler, C., Zhang, X., Flato, G., Wan, H., Li, G., & Castellan, A. (2022). Human influence on the 2021 British Columbia floods. *Weather and Climate Extremes*, *36*, 100441. https://doi.org/10.1016/j.wace.2022.100441

Weather and Climate Extremes 36 (2022) 100441

Contents lists available at ScienceDirect

Weather and Climate Extremes

journal homepage: www.elsevier.com/locate/wace

Human influence on the 2021 British Columbia floods

Nathan P. Gillett [a,*], Alex J. Cannon [a], Elizaveta Malinina [a], Markus Schnorbus [b], Faron Anslow [b], Qiaohong Sun [b], Megan Kirchmeier-Young [a], Francis Zwiers [b], Christian Seiler [a], Xuebin Zhang [a], Greg Flato [a], Hui Wan [a], Guilong Li [a], Armel Castellan [c]

[a] Climate Research Division, Environment and Climate Change Canada, Canada
[b] Pacific Climate Impacts Consortium, University of Victoria, Victoria, BC, Canada
[c] Meteorological Service of Canada, Environment and Climate Change Canada, Victoria, BC, Canada

ARTICLE INFO

Keywords:
Event attribution
Atmospheric river
Extreme precipitation
Streamflow
British Columbia
Flooding

ABSTRACT

A strong atmospheric river made landfall in southwestern British Columbia, Canada on November 14th, 2021, bringing two days of intense precipitation to the region. The resulting floods and landslides led to the loss of at least five lives, cut Vancouver off entirely from the rest of Canada by road and rail, and made this the costliest natural disaster in the province's history. Here we show that when characterised in terms of storm-averaged water vapour transport, the variable typically used to characterise the intensity of atmospheric rivers, westerly atmospheric river events of this magnitude are approximately one in ten year events in the current climate of this region, and that such events have been made at least 60% more likely by the effects of human-induced climate change. Characterised in terms of the associated two-day precipitation, the event is substantially more extreme, approximately a one in fifty to one in a hundred year event, and the probability of events at least this large has been increased by a best estimate of 45% by human-induced climate change. The effects of this precipitation on streamflow were exacerbated by already wet conditions preceding the event, and by rising temperatures during the event that led to significant snowmelt, which led to streamflow maxima exceeding estimated one in a hundred year events in several basins in the region. Based on a large ensemble of simulations with a hydrological model which integrates the effects of multiple climatic drivers, we find that the probability of such extreme streamflow events in October to December has been increased by human-induced climate change by a best estimate of 120–330%. Together these results demonstrate the substantial human influence on this compound extreme event, and help motivate efforts to increase resiliency in the face of more frequent events of this kind in the future.

1. Introduction

An atmospheric river (AR) event on November 14th and 15th 2021 brought two days of intense precipitation to southwestern British Columbia (B.C.). This event and associated antecedent conditions caused a number of landslides in the region, resulting in at least five fatalities. Floodwaters, landslides, wash-outs and bridge collapses caused by the event closed all the highways, pipelines and rail lines connecting Vancouver and southwestern B.C. with the rest of Canada for several days (Figs. S1 and S2), with some highways closed for weeks after the event. Key areas impacted by flooding included the Sumas Prairie area of Abbotsford where more than 1000 homes were flooded and thousands of farm animals died after a dike on the Sumas River was breached; the town of Princeton, where the Tulameen and Similkameen Rivers converge, which was flooded due to overtopping of levees; and the town of Merritt, which was completely evacuated due to the threat of inundation of the wastewater treatment facility and other hazards (these and other geographical features referred to in this paper are shown in Fig. S1). Insurance Bureau of Canada (2021) estimates the insured losses from this event as 450 million Canadian dollars, making this the most costly weather extreme in the province's history, but notes that the overall financial losses will be much higher, in part because many residents impacted by the event were not insured.

ARs are long, narrow, shallow filaments of concentrated water vapour transport typically found ahead of cold fronts in extratropical cyclones (Ralph et al., 2018; Douville et al., 2021). Sharma and Déry

* Corresponding author.
E-mail address: nathan.gillett@ec.gc.ca (N.P. Gillett).

https://doi.org/10.1016/j.wace.2022.100441
Received 31 January 2022; Received in revised form 10 March 2022; Accepted 22 April 2022
Available online 27 April 2022

(2020a, 2020b) report that the phenomenon is responsible for more than 90% of extreme rainfall in coastal regions of B.C. Two successive ARs impacted the coasts of southern B.C. and northern Washington state in mid-November 2021. A less intense event primarily impacted northern Washington state on 11th-13th November, followed by a more intense system that is the subject of this work. The orientation of these ARs was driven by a positive 500-hPa geopotential height anomaly that created a ridge over North America's Pacific coast (Fig. 1). Past studies have shown that the strength of this ridge determines the orientation of the AR's axis and the resulting latitude of landfall along North America's western coastline (Mundhenk et al., 2016; Sharma and Déry, 2020c).

Sharma and Déry (2020c) report a statistically significant upward trend in landfalling ARs over the west coast of B.C. and Alaska between 1979 and 2016. Based on this and other studies, the IPCC Sixth Assessment Report assessed that it was likely that an increase in AR activity in the eastern North Pacific had occurred since the mid-20th century, though no formal attribution assessment of this change was made (Douville et al., 2021). While the report found that an overall increase in extreme precipitation for the Western North America and North Western North American regions has not yet been observed or attributed, an increase in extreme precipitation averaged over the whole of North America was found to be attributable to human influence (Seneviratne and Zhang, 2021). Moreover, Sun et al. (2021) found that a number of stations in southwestern B.C. have exhibited statistically significant increasing trends in 5-day extreme precipitation.

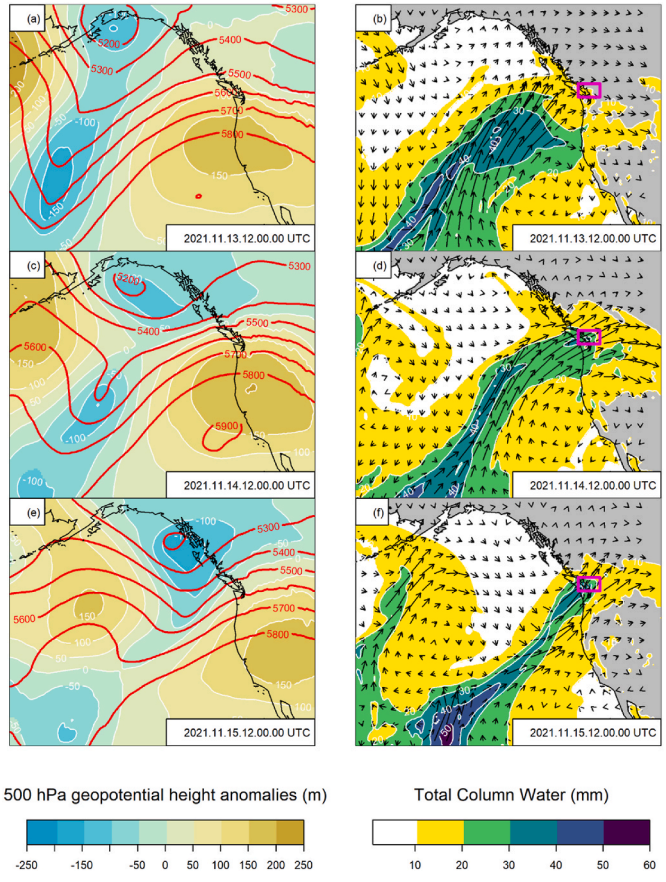

Fig. 1. Synoptic evolution of the AR from November 13th to 15th, 2021, shown in terms of geopotential height anomalies (left column) and total column water (right column), from ERA5. Red-colored contours show geopotential height, while vectors depict the vertically integrated vapour transport. The magenta rectangle in the right column shows the area used to calculate means of integrated vapour transport and precipitation in this study. (For interpretation of the references to colour in this figure legend, the reader is referred to the Web version of this article.)

There is a close link between landfalling ARs and extreme river discharge (Neiman et al., 2011; Sharma and Déry 2020b). For example, Sharma and Déry (2020b) show that AR-related maximum runoff in coastal B.C. watersheds is significantly higher than non AR-related runoff, and that 78% of flood-related disasters in B.C. between 1979 and 2016 are linked to ARs. Compared to other winter storms, AR storms typically transport relatively warm, moist air that raises the altitude of the 0 °C isotherm, or freezing level (Neiman et al., 2008; Kim et al., 2013; Warner et al., 2012). This results in more precipitation falling as rain (instead of snow) at high elevations and increased snowmelt, which often leads to runoff over a much larger catchment area than during a typical storm (Neiman et al., 2011; Guan et al., 2016). The combined rain-on-snow effect can increase extreme runoff and streamflow, resulting in increased flood hazard in temperate-climate mountain systems throughout the world (Freudiger et al., 2014; Li et al., 2019; McCabe et al., 2007; Musselman et al., 2018; Ohba and Kawase, 2020).

In this study we start by examining the AR event itself, characterised in terms of its vertically integrated vapour transport (IVT), before moving on to consider precipitation, and lastly examining streamflow during this event. In this way we start with the most well-understood aspects of the event, before moving on to consider streamflow, which is more closely related to the event's impacts, but which is influenced by a broader range of factors, including snowmelt and antecedent conditions. For each variable in turn we characterise the event, and its estimated return period, based on available observations, before estimating the contribution of human-induced climate change to any changes in this return period.

2. Integrated vapour transport

2.1. Event definition

ARs are generally characterised by their IVT. Our event definition is based on the AR scale developed by Ralph et al. (2019), which rates the severity of AR storms based on the duration of exceedances of IVT thresholds at a location. To define the event, we average 3-hourly IVT over a rectangular box covering parts of southwestern B.C. and northeastern Washington state between 48.25°N and 50.25°N, and between 120.5°W and 125°W, which encompasses the areas of heaviest precipitation associated with this event and the areas that were most impacted (Fig. 1, Fig. S1). In the Ralph et al. (2019) scale, an AR is assigned a categorical rating of 1 (primarily beneficial) to 5 (primarily hazardous) based on event maximum IVT exceeding thresholds of 250, 500, 750, 1000, and 1 250 kg m^{-1} s^{-1}, respectively. Storm duration is defined by Ralph et al. (2019) as the length of time that IVT continuously exceeds 250 kg m^{-1} s^{-1}; if the storm lasts less than 24 h, it is downgraded one category, and if it lasts for 48 h or more, it is upgraded one category. Storm-total precipitation and flooding have been found to be highly correlated with storm-total IVT integrated over the duration of the AR (TIVT), especially the upslope component of TIVT (Ralph et al., 2013), although it is not the only driver of precipitation variations (Mo et al., 2021). Hence, we characterise the intensity of each AR event using TIVT, taking into consideration storm orientation. To apply extreme value analysis, as described below, we only consider the strongest AR in each year. Our primary event attribution metric is thus the annual maximum TIVT value associated with ARs having a similar westerly trajectory as the observed event.

2.2. Observations and models

This study uses the ERA5 reanalysis (Hersbach et al., 2020) and its extension to 1950 (Bell et al., 2021) to calculate IVT (using data on levels from 1 000 hPa to 300 hPa) and characterise the event of interest. ERA5 has a higher horizontal resolution of 31 km, compared to 80 km in ERA-Interim, which allows it to represent synoptic-scale variability more realistically (Hersbach et al., 2020; Bell et al., 2021).

ERA5 has already been used for studies of ARs across the globe (e.g. Shu et al., 2021).

Fig. 1d shows IVT from ERA5 at 12:00 UTC on November 14th, 2021, which corresponds to the maximum intensity (>550 kg m^{-1} s^{-1}) of the second, stronger AR that hit the region during the flooding event. Following the Ralph et al. (2019) definition, the AR lasted 48 h, from 00:00 UTC on November 14th to 00:00 UTC on November 16th (Fig. 2a), and was rated a Category 3 storm. This rating is based on spatially-averaged IVT rather than IVT at individual ERA5 grid cells. The AR reached Category 4 at grid cells on the western edge of the event region near Vancouver Island, but Category 2 over the eastern, inland part of the region. Climatologically, ARs over the region come from southerly to westerly directions (Fig. 2b), with most having a south-westerly orientation. The November 14th storm was more westerly oriented (median angle of 246° during the event). This aligns with the east-west axis of the Fraser Valley, and hence is favourable for inland penetration and precipitation over the eastern portion of the region (e.g., coinciding with the flooding that occurred in Princeton and Merritt). Observed event-total precipitation in the eastern portion of the region (120.5°W to 121.5°W) is more highly correlated with annual maximum TIVT for ARs with a westerly orientation ($r = 0.6$, 90% Confidence Interval (CI): 0.39–0.75) than for those with a southwesterly ($r = 0.47$ CI: 0.23–0.66) or southerly ($r = 0.32$, 90% CI: 0.07–0.55) orientation. Similar sensitivity of precipitation and flooding to AR orientation in neighbouring Washington state was noted by Neiman et al. (2011).

When compared with the strongest event in each year since 1950 (Fig. 2c), irrespective of orientation, the TIVT of the November 14th AR was 111% of the average annual maximum. Based on a fit of the Generalised Extreme Value (GEV) distribution to annual maxima from 1950 to 2021, the magnitude corresponds to a 1 in 3.2 year event (90% CI: 2.5–4.1 year). Strong events in November 1990 and October 2003 were associated with the Skagit Basin/Sumas River floods (Hubbard, 1994), and the Pemberton/Sea to Sky floods (Sharma and Déry, 2020b) respectively. By this metric, the 2021 event was stronger than the typical strongest storm of the year, but weaker than a number of other events in the record. However, when our analysis is restricted to events with a westerly orientation (>240°), which exhibit stronger water vapour transport into the eastern portion of the lower Fraser Valley, the 2021 event has a TIVT of 180% of the average annual maximum. Based on this definition, the 2021 AR is estimated to be a 1 in 11.8 year event (90% CI: 7.8–17.9 year).

For event attribution and projection of future changes in AR storms over the region, observed annual maximum AR TIVT is compared with simulated TIVT from a 50-member initial condition large ensemble of the CanRCM4 (0.44° grid spacing) regional climate model forced by global CanESM2 simulations under historical and RCP8.5 forcings (Scinocca et al., 2016; Fyfe et al., 2017; Kirchmeier-Young et al., 2019). Whan and Zwiers (2016) found that CanRCM4, when supplied with lateral boundary conditions from ERA-Interim, was able to reproduce the spatial extent, intensity, and location of landfalling ARs along the west coast of North America well. The proportion of winter rainfall on days with ARs also closely matched observationally-constrained values. As a complement to results from CanRCM4, we also analyse initial condition ensembles from three CMIP6 global models with pre-calculated IVT or sufficient sub-daily pressure level data to calculate IVT during AR events: CESM2 (30) (Rodgers et al., 2021), MPI-ESM1-2-HR (10) (Müller et al., 2018), and MRI-ESM2-0 (5) (Yukimoto et al., 2019), each with simulations from 1850 (1950 for

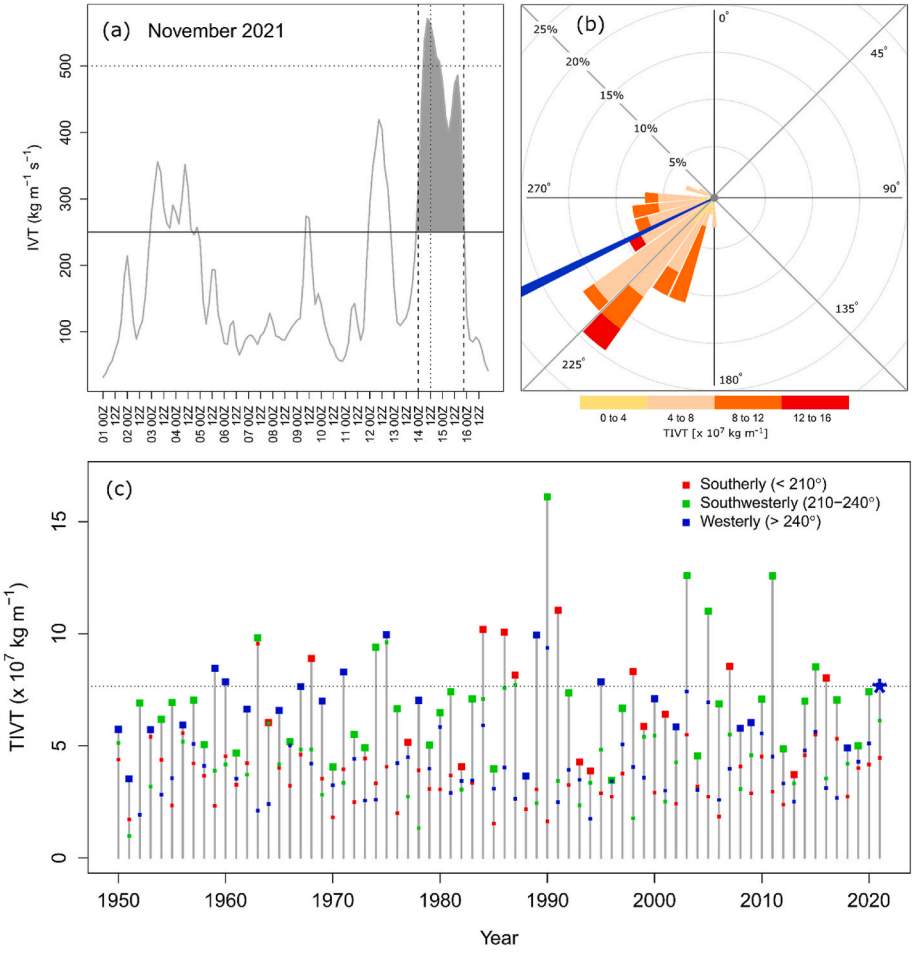

Fig. 2. (a) Time series (November 1st-16th, 2021) of IVT averaged over the event region shown in Fig. 1; vertical lines and shading show the duration of the AR (IVT ≥250 kg m^{-1} s^{-1} from November 14th 00:00 UTC to November 16th 00:00 UTC). (b) Directional histogram showing the orientation and strength of the strongest ARs in each year from 1950 to 2021; orientation of the November 14th AR is indicated in blue. (c). Time series of annual maximum TIVT for all ARs (vertical bars) and annual maximum TIVT for ARs with southerly (red), southwesterly (green), and westerly orientations (blue); each large square corresponds to the strongest AR in a given year. The blue asterisk and horizontal line indicate the strength of the November 14th, 2021 AR. (For interpretation of the references to colour in this figure legend, the reader is referred to the Web version of this article.)

MRI-ESM2-0) to 2100 under historical (Eyring et al., 2016a) and SSP3-7.0 (O'Neill et al., 2016) forcings, where ensemble sizes are indicated in brackets. Each of these global atmospheric models has a horizontal grid spacing of ~100 km.

2.3. Event attribution

To assess the degree to which human influence has affected the rarity of events like the November 14th AR, we regress simulated values of annual maximum TIVT during westerly ARs on decadal mean global near-surface air temperature (GSAT) anomalies using a nonstationary GEV model. Based on the fitted model, we calculate the probability of an event with a given magnitude under a climate with present day warming and a counterfactual pre-industrial climate with no human-induced warming. The regression takes advantage of the approximately exponential dependence of atmospheric moisture on temperature by expressing the logarithm of the GEV location and logarithm of the GEV scale parameter (El Adlouni et al., 2007) as linear functions of GSAT anomaly; the (scaled) hyperbolic tangent of the shape parameter – used to keep values between −0.5 and + 0.5 (Martins and Stedinger, 2000) – is similarly made to be a linear function of GSAT anomaly.

Given that results from GEV regression models can be sensitive to parameterisation and model structure, 15 alternative formulations of varying complexity (using different combinations of link functions for GEV parameters, as well as adopting models with stationary shape, or stationary scale and shape) were assessed for each climate model ensemble separately; based on the Akaike Information Criterion, the nonstationary model described above is recommended for each of the four climate model ensembles (Table S1). As a further check on model formulation, quantile regression models, which do not assume a parametric distribution for TIVT, were fitted to the climate model outputs. Results from GEV and quantile regression models are similar (Fig. S3), which lends further support to the use of the chosen GEV model. Confidence intervals for all quantities derived from the fitted models are determined by resampling from the pool of years with replacement, refitting the models, and calculating derived statistics 1 500 times.

Nonstationary GEV models are fitted to each climate model ensemble separately. Results for CanRCM4 are shown in Fig. 3; values of TIVT from ERA5 are shown for comparison. An AR like the observed event, with a westerly orientation and mean recurrence interval of 11.8 years in a climate with +1.09 °C warming since the pre-industrial (i.e., comparable to the amount of observed warming to 2011–2020; IPCC, 2021), would have been a 20.7 year event in the pre-industrial climate. This indicates that the probability of an AR event similar to that which started on November 14th has been increased by more than 60% by the effects of human-induced climate change (probability or risk ratio of 1.76, 90% CI: 1.64–1.93). Broadly consistent results are obtained from the other three global climate models (estimated probability ratios of 1.76, 1.38, and 2.42 for CESM2, MPI-ESM1-2-HR, and MRI-ESM2-0, respectively; Fig. S4); in all cases, confidence intervals exclude one, which indicates a robust human influence on AR event probability.

For CanRCM4, projected future changes in AR storm magnitude and rarity can be estimated from Fig. 3. For example, a 10-year event in the current climate is projected to be an approximately 8-year event with 1.5 °C global warming, a 7-year event with 2 °C warming, and a 5-year event with 3 °C warming, relative to the pre-industrial climate. Annual maximum TIVT in CanRCM4 scales with GSAT anomaly at a rate of ~12% per °C for all quantiles. A synthesis of multi-model projections is provided in Fig. S5 for present day recurrence intervals from 5 to 50 years. There is some indication that rarer events increase in frequency more rapidly with warming than less rare events in the multi-model ensemble. This result differs from CanRCM4 and is primarily driven by MRI-ESM2-0, which shows scaling of TIVT with warming similar to CanRCM4 for the present day 5-year recurrence interval (12% per °C) but greater sensitivity for rarer events (17% per °C for the 50-year recurrence interval). This is also reflected in the increase in risk ratio

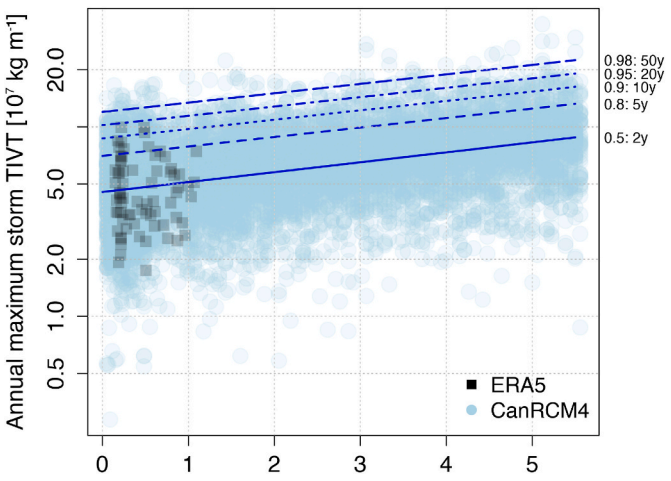

Fig. 3. Annual maximum TIVT for westerly-oriented ARs over the southwestern B.C. event region in the 50-member CanRCM4 large ensemble is shown against decadal mean GSAT anomaly relative to pre-industrial climate (1850–1900) in the associated CanESM2 global driving simulations (light blue dots). For reference, estimates of TIVT from ERA5 are also shown (black squares); here, observed GSAT anomalies relative to pre-industrial are obtained by adding the IPCC AR6 best estimate of +1.09 °C warming to ERA5 anomalies taken relative to the 2011–2020 mean. Blue lines show conditional TIVT quantiles corresponding to 2-year to 50-year recurrence intervals estimated from a GEV regression model conditioned on GSAT anomaly. Each dot (or square) shows annual maximum TIVT and GSAT anomaly values for one year. (For interpretation of the references to colour in this figure legend, the reader is referred to the Web version of this article.)

with event rarity for MRI-ESM2-0 (Fig. S4). Overall, projected increases in the frequency and magnitude of AR events with future warming are consistent with those simulated in the past, which enhances our confidence in the attribution of the November event.

3. Precipitation

3.1. Event definition

We focus primarily on precipitation averaged over the same box in southwestern B.C. as used for the IVT analysis (Fig. 4). This box encompasses the regions of highest precipitation during the November 14th-15th event, as well as covering the locations where the biggest impacts were experienced. We focus primarily on 2-day total precipitation beginning at 00:00 UTC on 14th November, which aligns with the 48-h period in which the AR event occurred (Fig. 2a), and includes most of the precipitation which fell during the event.

3.2. Observations and models

In this study we use two precipitation products: the ERA5 reanalysis (Hersbach et al., 2020), and its extension back to 1950 (Bell et al., 2021); and the Canadian Precipitation Analysis (CaPA; Lespinas et al., 2015; Fortin et al., 2018; Gasset et al., 2021). The former extends further back in time, making it more suitable for event attribution, while the latter is higher resolution, and better for characterising precipitation variations on a small scale. Although ERA5 does not assimilate gauge measurements of precipitation for most of its length (Hersbach et al., 2020; Bell et al., 2021), Hersbach et al. (2020) demonstrate that monthly variations in precipitation in ERA5 since 1979 correlate well with a gridded analysis of satellite and gauge observations in the area of interest, and Bell et al. (2021) demonstrate that the correlation of monthly precipitation in ERA5 with gridded gauge measurements is high in western North America and similar both before and after 1979. However, we note that Rivoire et al. (2021) find differences in the simulation of

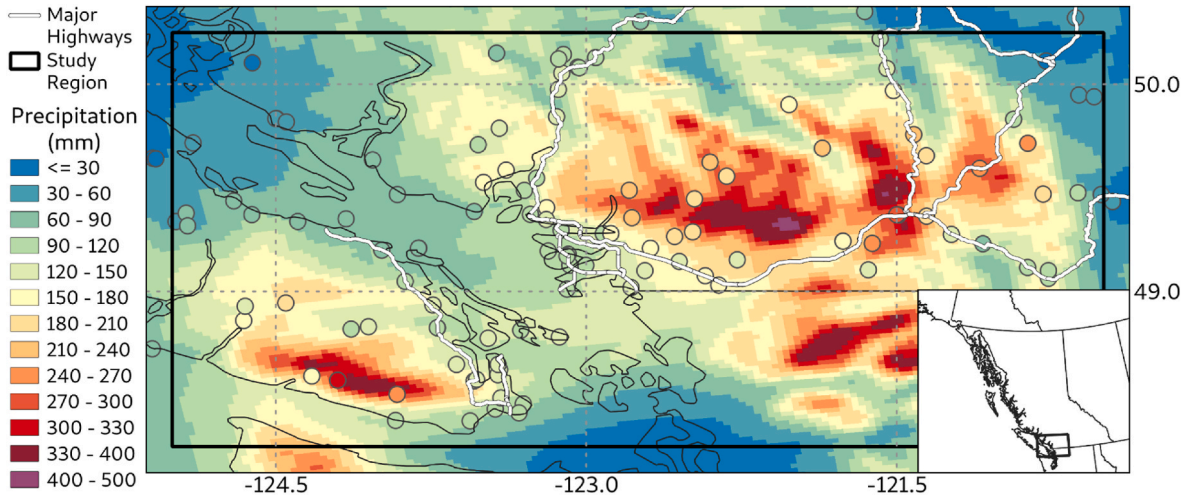

Fig. 4. Two-day total precipitation for November 14th-15th (00:00 UTC November 14th 00:00 UTC November 16th), from the 2.5-km version of the Canadian Precipitation Analysis (CaPA; colours) and from gauges (circles). The black rectangle indicates the area used to calculate averages of IVT and precipitation in this study. (For interpretation of the references to colour in this figure legend, the reader is referred to the Web version of this article.)

extremes between ERA5 and a gridded precipitation product in northwest North America. Hence, for comparison we also use the 10-km Regional Deterministic Prediction System version of CaPA, which is higher resolution than ERA5, assimilates a large number of gauge observations over Canada and the United States, and is available since 1980 (Lespinas et al., 2015; Fortin et al., 2018; Gasset et al., 2021). A 2.5-km version of CaPA is also used for characterising spatial variations, but the dataset began only in 2016 and is therefore too short for event attribution (Fortin et al., 2018). We also compare precipitation totals with rain gauge observations from Environment and Climate Change Canada, B.C. ministries and BC Hydro, the province's electrical utility.

Fig. 4 shows the total precipitation observed on November 14th-15th over the region of interest from the 2.5-km version of the CaPA analysis and rain gauge observations. There is a generally good correspondence between the rain gauge observations and the 2.5-km CaPA analysis over this period. There is also a good correspondence between the gauge observations and the 10-km CaPA analysis (Fig. S6a), but less good correspondence with the coarser resolution ERA5 (Fig. S6b). Two-day gauge precipitation totals reached 312 mm on southwest Vancouver Island while a maximum in the 2.5-km CaPA analysis of more than 400 mm was seen north of the Fraser Valley (Fig. 4). At Coquihalla Summit, near some of the most critical infrastructure impacts, a gauge total of 243 mm was recorded.

Fig. 5 shows cumulative precipitation from October 1st to November 30th each year averaged over the box in Fig. 4, based on the ERA5 reanalysis. Similar results were obtained from the CaPA analysis (Fig. S7). Individual extreme precipitation events correspond to periods where the cumulative precipitation curves rise steeply. The two-day precipitation from November 14th-15th 2021 was clearly unusually high (bold red line): it was exceeded only by events in 1955, 1968, and 2003 (see also Fig. S8). Fig. 5 also shows that cumulative precipitation immediately prior to the November 14th-15th AR event was already substantially higher than average. Based on Fig. S8, the 2021 event was weaker in ERA5 than in the higher resolution 10-km CaPA analysis - this is also apparent from Fig. S6, and might result from topographic effects being better simulated in the 10-km CaPA analysis.

Fig. S9 shows the distribution of RX2day in ERA5 between 1950 and 2021, and in CaPA between 1980 and 2021. The 2021 event has an estimated return period of 45 (90% CI: 18–120) and 100 (90% CI: 41–311) years, based on the ERA5 and CaPA datasets respectively, where uncertainties were estimated by bootstrap resampling years prior to 2021 with replacement 1 000 times and the 2021 event was added to each sample (Fig. S9). Hence when characterised in terms of precipitation, the event was substantially more extreme than when characterised in terms of IVT. However, precipitation is driven by net moisture convergence rather than by IVT itself (Mo et al., 2021). Based on ERA5, an analysis of 2-day IVT convergence over the southwestern B.C. box indicated that annual maximum 2-day IVT convergence and RX2day are

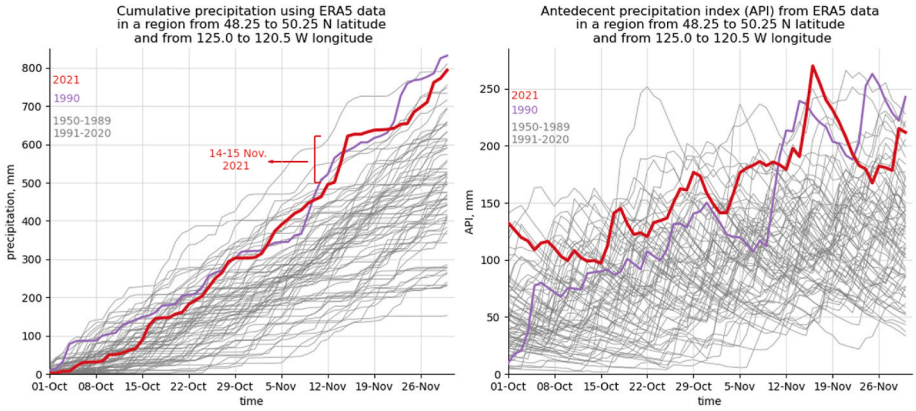

Fig. 5. Cumulative total precipitation averaged over the southwestern B.C. box shown in Fig. 4 from October 1st each year since 1950 from the ERA5 reanalysis (left). Antecedent precipitation index (Section 4.2) over the same region is also shown (right). Values for 2021 are shown in bold red, and 1990 is shown in purple for comparison. (For interpretation of the references to colour in this figure legend, the reader is referred to the Web version of this article.)

highly correlated (r = 0.92, 90% CI: 0.87–0.95). Furthermore, when characterised in terms of net moisture convergence, the November 2021 event had a very similar return period (44, 90% CI: 24–153 years) to that obtained for RX2day. More detailed study of the moisture convergence associated with this event, which depends on the interaction between the large-scale flow and the small scale topography, is beyond the scope of the present study.

To examine how much human influence contributed to the probability of the observed November 14th-15th 2-day precipitation extreme, we examined the distribution of annual maximum 2-day total precipitation (RX2day) in concatenated historical (Eyring et al., 2016a) and SSP2-4.5 (O'Neill et al., 2016) simulations from 166 simulations of 22 CMIP6 models (Table S2), using ESMValTool v2.4 (Eyring et al., 2016b). After re-gridding model daily precipitation output onto a 0.5° × 0.5° grid and area-averaging over the box shown in Fig. 4, we calculated annual maximum running 2-day total precipitation (RX2day) in the models and in ERA5. Comparing the distribution of RX2day in the CMIP6 models with ERA5 indicates that the models have a mean RX2day which is 20 mm less than ERA5. Hence, to reduce the effects of biases in mean RX2day in the models, we divide by mean RX2day over the 1950–1969 period separately for the observations and each individual simulation, to calculate a normalised RX2day (1950–1969 is the earliest 20-year period available in ERA5). To assess the contribution of human influence, the distribution of normalised RX2day anomalies over a 20-year period centred on 2021 (2011–2030), was compared with the distribution of normalised RX2day over the quasi-preindustrial 1850–1900 base period.

3.3. Event attribution

Fig. 6 shows the distribution of simulated RX2day anomalies over the 1850–1900 base period in green, along with the distribution in the 20-year present-day period centred on 2021 (2011–2030) in brown. GEV distributions fitted to the model output using L-moments for each period were found to fit the simulated values well (Fig. 6, top right). The distribution of RX2day for the present day is clearly shifted towards higher values compared to the 1850–1900 base period (Fig. 6). The magnitudes of the 2021 and 1955 events in ERA5 are also indicated on the plot for comparison. For events with a magnitude at least as large as that of the 2021 event, the ratio of their probability in the current climate compared to that in the base period, or risk ratio, is 1.45 (90% CI: 1.01–1.84). Hence our analysis indicates that human influence has increased the probability of a 2-day precipitation event at least as large as that in 2021, and the best estimate of this increase in probability is 45%. This risk ratio, and the results shown in Fig. 6, were obtained by weighting each individual simulation equally, even though ensemble sizes differed between models. Similar distributions (Fig. S10) and a similar risk ratio, albeit with wider uncertainties (1.40 90% CI: 0.85–2.17) were obtained using output from only the nine CMIP6 models with ensemble size greater than two (Table S2) and weighting simulations such that each model had equal weight. Moreover, broadly similar risk ratios, ranging from 1.18 to 1.92, were obtained from individual models with ensemble size of at least 10 (Table S2).

Fig. 6 also shows the simulated distribution of RX2day anomalies for the study area over the 2081–2100 period under SSP2-4.5, which is associated with a best estimate warming of GSAT, relative to 1850–1900, of 2.7 °C (IPCC, 2021). As expected, the distribution of RX2day for this period has a higher mean and also a higher spread (larger scale parameter) than the corresponding distributions for the base period or present day. The risk ratio for 2081–2100 is 3.16 (90% CI: 2.49–4.01) for an event of at least the magnitude of the 2021 event, relative to the 1850–1900 base period, or 2.18 (90% CI: 1.73–3.09) relative to the present day. Hence by the end of the century under the SSP2-4.5 scenario, extreme precipitation events comparable to that observed in November 2021 are expected to occur two to four times more frequently than in the preindustrial climate.

4. Streamflow

The high streamflow and associated flooding which occurred during the November 2021 event were influenced not only by the extreme 2-day precipitation, but also by other factors including snowmelt and antecedent conditions. Hence in this section we start by characterising the hydrometeorological conditions relevant to streamflow, before discussing mechanisms driving the streamflow during this event, and moving on to discuss observations of streamflow and event attribution.

4.1. Characterization

We characterise the hydrometeorology of the 2021 AR event using point observations of precipitation, snow water equivalent (SWE), and streamflow collected at meteorological and hydrometric sites in

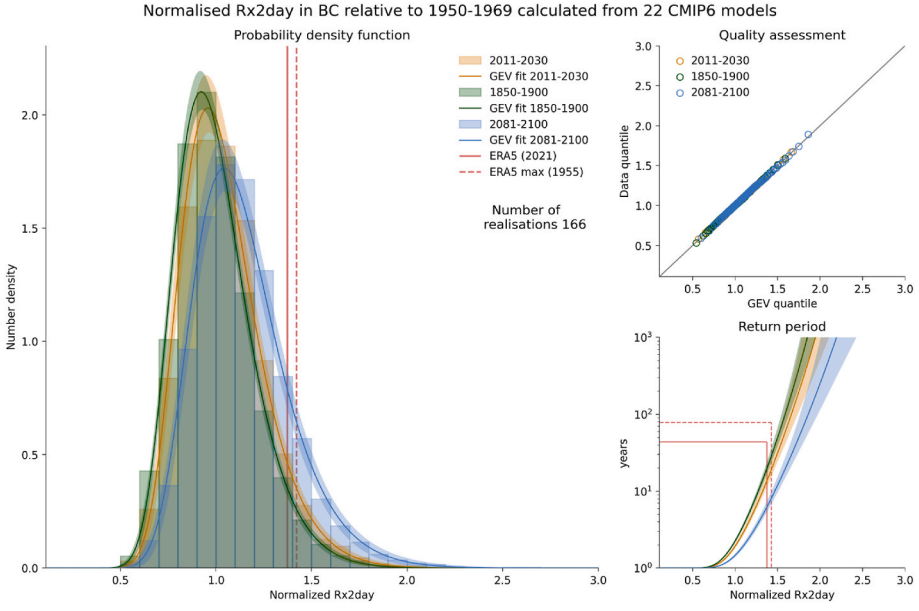

Fig. 6. RX2day normalised relative to 1950–1969 calculated from 166 concatenated historical and SSP2-4.5 simulations of 22 CMIP6 models (left). Green, brown and blue histograms show 1850–1900, 2011–2030 and 2081–2100 periods respectively. Curves are fitted GEV distributions, with associated 90% confidence ranges. Confidence ranges were constructed by bootstrap resampling 166 simulations with replacement 5 000 times. Fitted GEV location parameters were 0.91, 0.94 and 1.03, scale parameters were 0.18, 0.18 and 0.21, and shape parameters were 0.08, 0.07 and 0.06 for each of the three periods respectively Solid and dashed red lines show the magnitudes of the 2021 and 1955 events respectively. The top right panel shows the data quantile plotted against the GEV quantile to assess the quality of the fit for each period respectively. The bottom right panel shows the return period for an event of at least the magnitude shown on the x-axis, for each of the three periods, based on the GEV fits. Solid and dashed red lines show the magnitude (x-axis) and estimated return period (y-axis) of the 2021 and 1955 events respectively, from ERA5. (For interpretation of the references to colour in this figure legend, the reader is referred to the Web version of this article.)

southwestern B.C. (Fig. S11). As an example, observations from monitoring sites located in the Chilliwack basin are presented in Fig. 7. Precipitation began during the evening of 13th November and continued unabated until around 01:00 UTC on 16th November (Fig. 7a). The landfalling AR brought substantially warmer air to the region and the air temperature rose 8 °C from a low of −2.4 °C on the morning of 14th November to a high of 5.6 °C in the afternoon, and air temperature remained above 0 °C until just past 00:00 UTC on 16th November (Fig. 7c). Prior to air temperature rising above zero, precipitation contributed to increased SWE, causing SWE to rise 35 mm just before the onset of melt (Fig. 7b). Although local air temperature rose above freezing on the morning of 14th November, around 4–6 h was needed for the snowpack to warm and reach saturation, such that snowmelt did not begin until early afternoon on 14th November. Melt continued until the evening of 15th November.

Streamflow began to rise shortly after the onset of melt and reached a peak at about 23:00 UTC on 15th November, coincident with the cessation of both melt and precipitation (Fig. 7d). Total melt and cumulative precipitation over the 48-h period ending on November 16th, 08:00 UTC, were 104 mm and 178 mm respectively. The effective cumulative precipitation (melt plus precipitation) was 282 mm with a snowmelt contribution (melt ratio) of 37%. Results for stations in the Coldwater (Fig. S12) and Similkameen (Fig. S13) basins indicate that the hydrometeorological evolution of the storm event had very similar characteristics throughout the region. However, the more leeward Coldwater basin had lower 48-h effective precipitation (126 mm) and a lower melt ratio (17%), and the Similkameen, which is further inland, had a similar 48-hour effective precipitation (116 mm), but an even lower melt ratio (14%). These results demonstrate that the hydrological impacts of the AR event were driven by rain-on-snow conditions, where streamflow was generated by precipitation (predominantly as rainfall) augmented by snowmelt associated with a rapid rise in temperatures over the affected area.

4.2. Mechanisms

Although the importance of precipitation in flood generation cannot be overstated, basin state is also an important factor (Merz and Blöschl, 2003; Winkler et al., 2010). For instance, high antecedent soil moisture can condition a basin for increased flood magnitude (e.g. Wasko and Nathan, 2019; Wasko et al., 2020), and in rain-on-snow events, the amount of runoff generated depends upon snowpack state and the amount of energy available for melt (Würzer et al., 2016; Trubilowicz and Moore, 2017). Therefore, we explore not only the effect of precipitation which fell during that event, but also snowmelt and antecedent conditions.

4.2.1. Precipitation and runoff efficiency

The influence of precipitation is assessed by comparing 48-h total streamflow and precipitation observed during the fall period (October-November-December; OND) for six basins upstream of hydrometric gauge sites (Fig. S11, Table S3). The analysis is restricted to peak discharge events in the OND season as these are presumed to be dominated by the same mechanisms as the AR event under study (i.e., rainfall-driven with a varying contribution from snowmelt). A 48-h period is selected as this corresponds to the duration of the 2021 AR storm event. For each year we identify the maximum daily discharge during the OND period and extract the corresponding 48-h discharge and precipitation (for the 48-h period ending on the day maximum discharge is observed). Basin-average daily precipitation is estimated from the 10-km CaPA analysis (1980–2021) and daily discharge is converted to specific discharge by dividing by the basin area (Table S3).

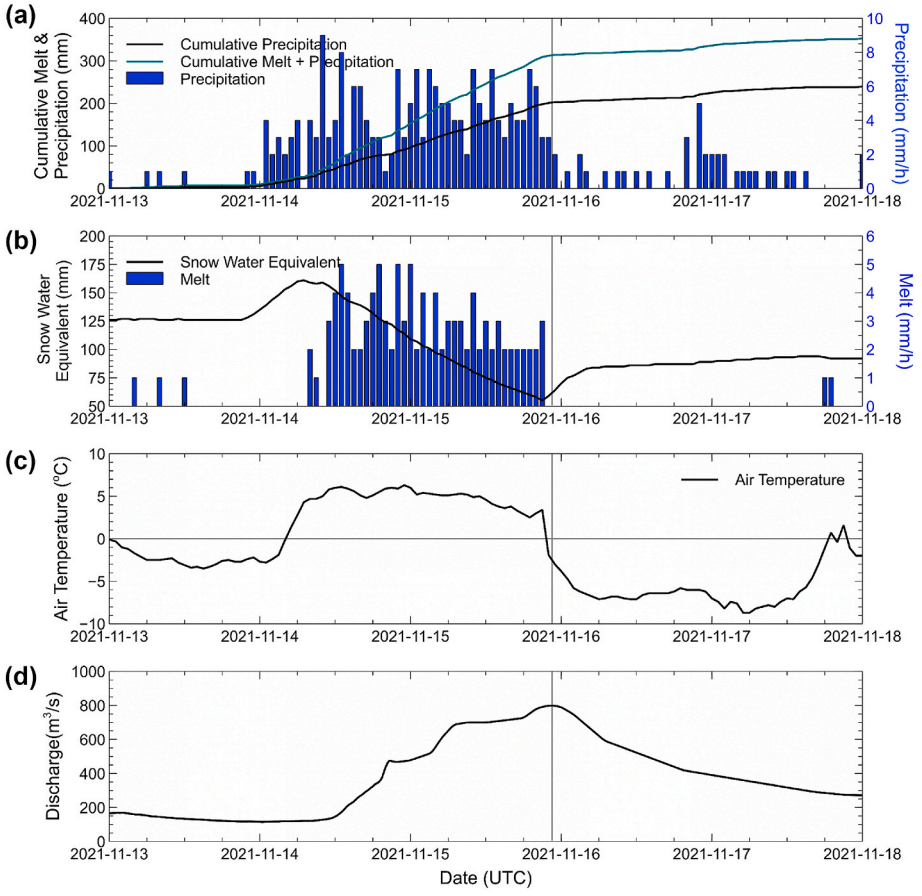

Fig. 7. Hydro-meteorological conditions for the Chilliwack basin showing a) (top) hourly precipitation, cumulative precipitation, and cumulative melt plus precipitation; b) (second row) hourly SWE and melt; c) (third row) hourly air temperature; and d) (bottom) hourly streamflow. Precipitation, SWE and melt data are from ASWS 1D17P (Chilliwack River; 1 600 m elevation), and streamflow data are from Water Survey of Canada gauge 08MH001 (Chilliwack River at Vedder Crossing). All data are plotted for the period November 13th, 2021 00:00 UTC to November 18th, 2021 00:00 UTC.

Historical hydrometric data from Water Survey of Canada (WSC) is only available up to 2019 and streamflow data for years 2020 and 2021 are based on provisional real-time hydrometric data that has not yet been subject to quality control. We also use the runoff efficiency, which is defined as the ratio of discharge to precipitation, to reflect the variation in basin state and storm characteristics between events. Lower runoff efficiency would be indicative of conditions causing delayed or dampened runoff (i.e., dry soil and/or cold, dry snowpack, snowfall and snow accumulation) and higher runoff efficiency would be indicative of conditions facilitating rapid runoff (wet soil and/or a warm, saturated snowpack, and rainfall) potentially augmented by snowmelt (Guan et al., 2016).

A strong west-east precipitation gradient is evident, where precipitation and specific discharge values are much higher for windward basins (Nooksack, Chilliwack and Coquihalla) as compared to leeward basins (Coldwater, Similkameen and Tulameen) (Fig. 8). In all six basins annual maximum peak OND discharge increases with the magnitude of event precipitation (Fig. 8), and associated Spearman rank correlation coefficients are statistically significant at the 5% level in all cases. Both 48-h discharge (Q_{48}) and 48-h precipitation (P_{48}) volume in 2021 rank in the top two events of all observed years (Fig. 8 and Table S4). However, there is considerable variation in runoff efficiency (for a given volume of precipitation, discharge increases with increasing runoff efficiency) (Fig. 8). Indeed, in all six basins many of the largest OND discharge events have been the result of relatively modest precipitation coupled with high runoff efficiency, typically in excess of one (suggesting a substantial contribution from snowmelt). However, runoff efficiencies for the 2021 AR event are modest, ranging from 0.43 (Similkameen) to 0.76 (Coldwater) (Table S4).

4.2.2. Antecedent conditions

The study region is topographically complex, and winter precipitation can occur as either snow or rain (Whitfield et al., 2002; Fleming et al., 2007). As such, we use both soil moisture and SWE as complementary indications of the antecedent state of the basin. In the absence of modelled or direct soil moisture observations we use the antecedent precipitation index (API) as a proxy (see Supplement for a description of the API). The 30-day API for each year from 1950, based on ERA5, is presented in Fig. 5. The API trace for 2021 demonstrates that the region experienced wet conditions throughout October and the start of November. The resulting API on November 13th, 2021 was one of the highest on record, suggesting that local watersheds were experiencing unusually high soil wetness conditions (i.e. limited storage capacity) prior to AR landfall. Results are similar when API is estimated using precipitation from the CaPA analysis (Fig. S7).

Antecedent SWE is examined using observations from snow pillow sites in both the SNOw TELemetry (SNOTEL) network in the United States (Natural Resources Conservation Service, 2022) and the Automated Snow Weather Station (ASWS) network in British Columbia (Ministry of Environment and Climate Change Strategy, 2009). Antecedent SWE on November 13th, 2021, observed at snow pillow sites (with records $\geq$ 20 years), was higher than normal, but not extreme, and ranged between the 70th and 90th percentile of historical daily observations for the 3-day period centred on November 13th (Fig. S14a).

4.2.3. Snowmelt

Melt over the duration of the AR event is examined using both point melt rates estimated from snow pillow observations and distributed melt rates from the Snow Data Assimilation System

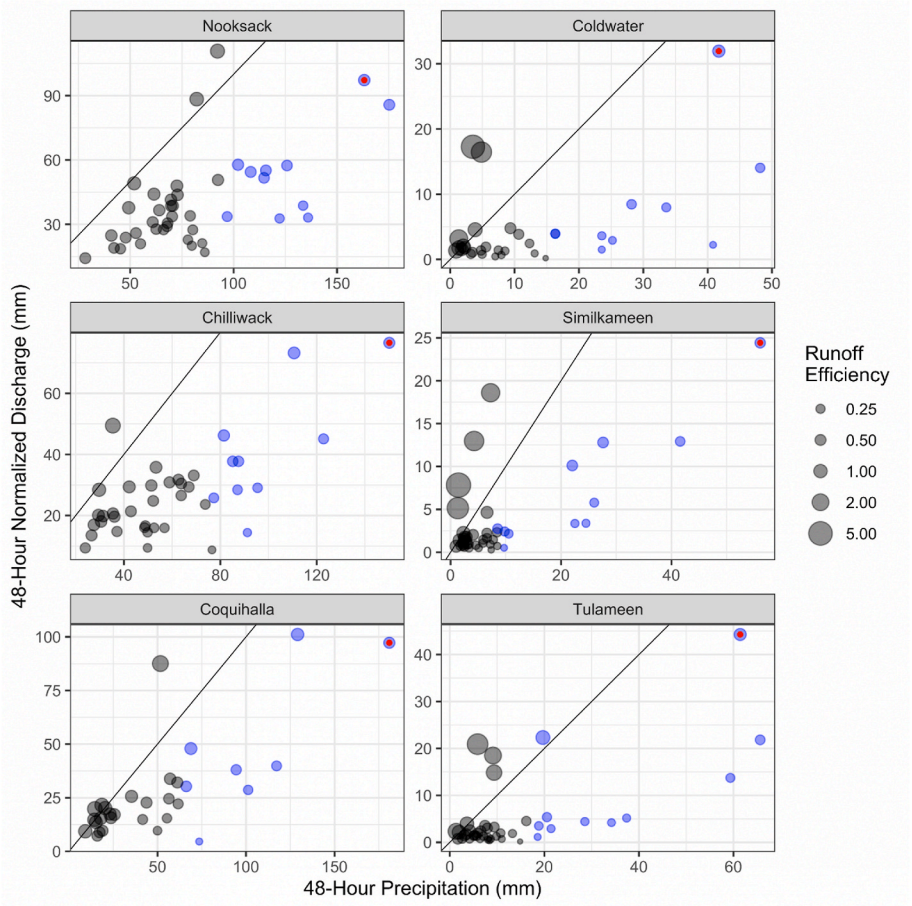

Fig. 8. Precipitation, discharge and runoff efficiency for the Chilliwack, Coldwater, Coquihalla, Nooksack, Similkameen, and Tulameen Rivers in October–December. The 2021 event is indicated by a red dot and large precipitation events (those in the upper quartile) are shown in blue. The 1:1 relationship is indicated by the solid line and events above this line have a runoff efficiency greater than one. (For interpretation of the references to colour in this figure legend, the reader is referred to the Web version of this article.)

(SNODAS) (Carrol et al., 2001; National Operational Hydrologic Remote Sensing Center, 2004). SNODAS melt products are only available as 24-h totals for the period up to 05:00 UTC, hence we report 48-h totals for the period November 14th 05:00 UTC to November 16th 05:00 UTC. Melt rates are highest (in places >100 mm) within a belt along the windward side of the southern Coast Mountains and Cascade Range (Fig. S14b). The spatial distribution of melt from SNODAS generally agrees with that of the pillows, although SNODAS melt appears slightly overestimated. Snow melt was widespread within the windward belt of the Coast and Cascade Mountains and occurred at all but the highest elevations in the Coast Mountains, indicating that the melting/freezing level had risen to at least ~2000 m (e.g., 36 mm of melt was observed at the Hart's Pass SNOTEL site, which is at an elevation of 1978 m). This also indicates that precipitation widely occurred as rain, not snow. Total melt decreases farther inland to the east and melt becomes negligible on the leeward side of the Coast Mountains in the northern portion of the domain.

The contribution of snowmelt to the effective precipitation (precipitation plus snowmelt) for the 48-h period ending November 15th, 2021, at snow pillow sites, is shown in Fig. S14c. For most sites located south of 50°N, melt ratios were between 10% and 25%. Although melt ratios were highest (exceeding 50%) at two SNOTEL sites located in the lee of the Cascade Mountains (Muckamuck and Salmon Meadows), effective precipitation in this region was quite low (<48 mm). Melt ratios at windward sites with effective precipitation exceeding 150 mm ranged from 17% (ASWS 1D19P, lower Fraser) to 36% (ASWS 1D17P, Chilliwack River).

4.2.4. Wildfire

Southern B.C. saw many large wildfires in 2021 (Fig. S2), some near areas of heavy rainfall in the November event. Therefore, we also consider the possible influence of recent wildfires in the region on the extent and magnitude of flooding. There are many mechanisms through which wildfires can impact the local hydrologic response and susceptibility to debris flows. For example, loss of the vegetation canopy can result in increased snowmelt and rainfall reaching the ground, loss of litter can decrease water storage, loss of root structures can decrease ground stability, and reductions in infiltration and altered soil characteristics can increase runoff (Parise and Cannon, 2012; Winkler et al., 2010). Although the timing depends on many parameters and can be site specific, recovery of hydrology-relevant factors following a fire can take several years (Ebel and Martin, 2017). Parts of southern B.C. have experienced post-fire debris flows and landslides, particularly after the 2003 fire season, triggered by moderate-to-heavy rainfall, high peak flow, and/or spring snowmelt (Jordan, 2015). Considering the basins defined in Section 4.2.1, the Similkameen Basin upstream of Princeton had almost 8% of its area burned by wildfires in B.C. in 2021 and the Coldwater Basin upstream of Merritt had about 15% burned (Fig. S2b). While we cannot rule out a possible influence on runoff efficiency in these basins, no relationship is apparent between percent of basin burned and runoff return period or runoff efficiency for the 2021 event (Figs. S2c and d). Moreover, we can conclude that for other basins which experienced impacts, such as the Coquihalla and Sumas/Nooksack basins, the small areas burned there preclude a significant role for wildfire in driving runoff during the event.

Many road impacts (e.g., debris flows, washouts, flooding) occurred either in or adjacent to areas burned during the 2021 fire season, representing about 25% of reported road impacts in our inventory and almost 40% of the impacts when focusing on an interior region (Fig. S2a). While previous literature (Jordan, 2015; Parise and Cannon, 2012) suggests that recently burned areas may be more susceptible to debris flows during subsequent heavy rainfall and streamflow events, more in-depth analysis of site-specific data, which is beyond the scope of the present study, would be required to demonstrate whether or not a causal link is present here.

4.2.5. Synthesis

Despite high antecedent wetness, above average snow accumulation and a contribution from snowmelt, along with a small possible contribution from recent wildfire in certain basins, runoff efficiency for the 2021 event does not rank as extreme (Table S4). Rather it ranges from normal to high, but was not atypical compared to other high streamflow events. From an analysis of snow pillow data from several sites in southwestern B.C., Trubilowicz and Moore (2017) noted that for large rain-on-snow events, although snowmelt enhances the amount of water available for runoff (on average by 25%), the total amount of rainfall is the most important control on water available for runoff. This is also consistent with the findings of Li et al. (2019), who determined that runoff generated during rain-on-snow events along the west coast of the United States is dominated by rainfall. For large precipitation events, which we define as those falling in the upper quartile for each location, runoff efficiency appears asymptotically constrained such that runoff variation between events is predominantly driven by precipitation intensity (Fig. 8). Hence, although runoff and streamflow were affected by antecedent conditions and the occurrence of snowmelt, the magnitude and extent of flooding during the 2021 AR event were primarily the result of extreme precipitation, a large proportion of which was undoubtedly in the form of rain.

4.3. Observations

Most streamflow gauges reached their peak flow for the event on 15th November, generally around the time the heavy rainfall ended. Fig. 9 displays return periods for the event peak flow at natural flow locations (locations without dams or other flow regulations upstream). The return periods were estimated using a GEV distribution fitted with an L-moments approach to annual peak flows at each station location. The 2021 event was moderately extreme at most locations, with several stations showing more extreme values. Of the 32 unregulated stations in Fig. 9, 20 experienced at least a one in 20-year event, 11 at least a one in 50-year event, and 5 experienced more than a one in 100-year event. These return periods are highly uncertain (as discussed below), but can provide a general sense of the event. Of the 32 stations, 16 experienced an event peak flow greater than any value in the prior station record. Half of those stations saw an increase of more than 25% over the prior maximum and a quarter saw an increase of over 50%. The drainage basins contributing to each streamflow gauge location are shown in Fig. 9.

Small samples and different record lengths at different locations are sources of uncertainty for placing the streamflow event in the historical context. The record lengths of the stations shown here range from less than 10 years of data to more than 50 years (Fig. S15). The robustness of a comparison to previous records and the fit of a GEV distribution can be hindered by limited data. Observations of extreme streamflow are also uncertain as they are extrapolated using an existing relationship between water level and streamflow. Further, the observations of the 2021 event may not be accurate at many locations as geomorphic changes in the channel during the flooding event may have changed the relationship between water level and streamflow. Missing data at a few locations for periods during the event also contribute to lowering confidence in some observations. Hence, the event streamflow results presented here should be interpreted with caution.

4.4. Event attribution

To assess the role of human influence in the occurrence of events like the November 15th extreme streamflow, we compared the magnitudes of different return period events for the 1950–1969 and 2011–2030 climate states using hydrologic simulations driven by the CanESM2 large ensemble. The simulations from the CanESM2 large ensemble, which also provided boundary conditions to the CanRCM4 dynamical downscaling used in the IVT analysis, were statistically downscaled and bias

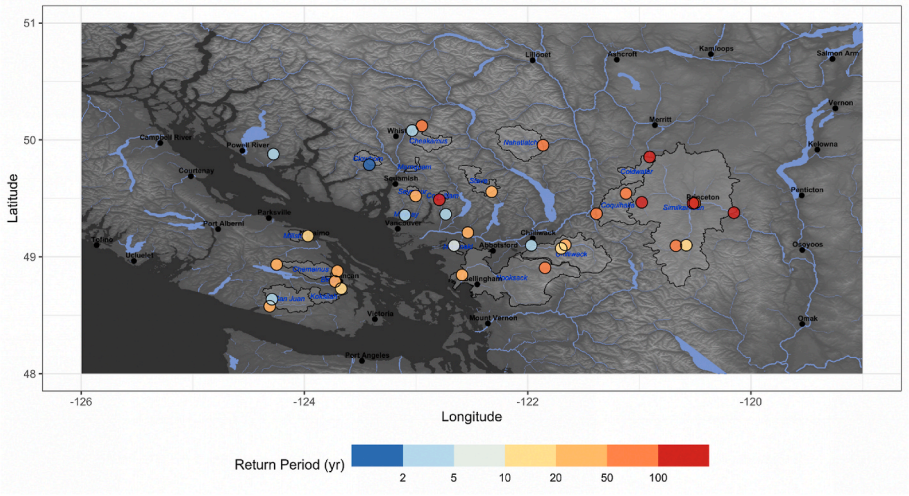

Fig. 9. Streamflow return periods for the November 2021 peak flows at hydrometric stations. Streamflow is unregulated at all stations, except for the two sites in the Nooksack. Drainage areas for each gauge are outlined; for nested basins, the area is only shown for the most downstream gauge.

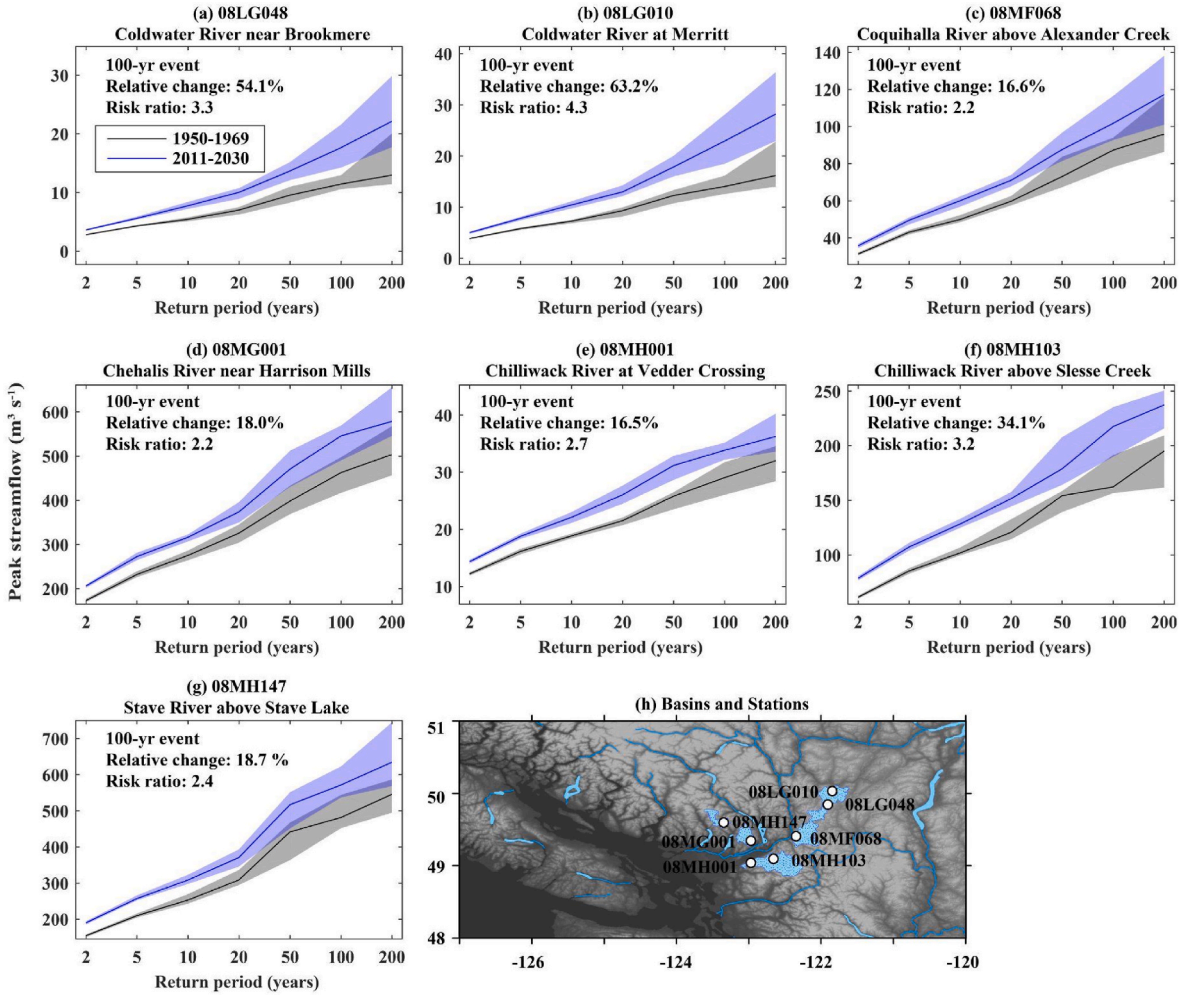

Fig. 10. Flood frequency plots showing estimated October-November-December period (OND) peak streamflow for 1950–1969 (black) and 2011–2030 (blue) against return period in seven locations, based on empirical fitting. Shading denotes the 90% confidence interval. The relative change in the magnitude of the 100-year OND peak streamflow between 1950-1969 and 2011–2030 and the risk ratio comparing the probability of the 100-year OND peak flow in the 1950–1969 climate state between the two periods are shown in the upper left corner. (h) Map showing the locations used for the analysis. (For interpretation of the references to colour in this figure legend, the reader is referred to the Web version of this article.)

corrected to a high-resolution (0.0625° latitude by 0.0625° longitude) gridded temperature and precipitation dataset (Werner and Cannon, 2016; Werner et al., 2019) and then used to drive the VIC-GL hydrological model (Schnorbus, 2018). A benefit of using a large ensemble is a more statistically robust estimation of the return periods of large events. Although the analysis of streamflow gauge observations was based on the annual peak flow, which is a very commonly used metric, the resolution and data availability of the hydrological simulations allow the event definition to be more specific to the November 2021 event. The peak flows in October-November-December (OND) were extracted for each year and each model run of the large ensemble, resulting in 900 streamflow values for each period (20 years for each of 45 ensemble members) at each grid point. The 2-, 5-, 10-, 20-, 50-, 100- and 200-year return levels during the earlier 20-year period (1950–1969) and current (2011–2030) periods were estimated empirically using the function "quantile" from the R stats package (R Core Team, 2019). Note that we could not use an earlier base period because the available simulations started in 1950, but anthropogenic warming to 1950 was only about 0.2 °C (Eyring et al., 2021), hence we use this period as an approximation for preindustrial for our hydrological analysis. The confidence intervals for each quantile were estimated using a bootstrapping approach, sampling 1 000 times.

Here we present the flood frequency results for seven locations that are 1) unregulated, 2) located within the Fraser Basin, and 3) have a drainage area >285 km^2 (i.e., about 10 model grid cells). The results are summarized graphically as flood frequency curves in Fig. 10. Flood magnitudes for all return periods in the current climate are larger than in the 1950–1969 climate at all seven locations. The best estimates of the 100-year OND peak flow in the current climate are 16.5–63.2% larger than those in the 1950–1969 period, depending on location. For an event with the magnitude of the 100-year OND peak flow in the 1950–1969 climate, the ratio of its probability in the current climate compared to the 1950–1969 period, or risk ratio, is 2.2–4.3, depending on location. At all seven locations, the lower bound of the 90% confidence interval on the risk ratio is greater than one, indicating an increase in the likelihood of the event in the warmer climate. However, at some locations, these uncertainty ranges only just exceed one and changes in the sample size or event definition may change the attribution result. Overall, the results indicate that the 100-year OND peak flows in the 1950–1969 climate now occur roughly 2–4 times as frequently due to the effects of human-induced climate change.

5. Conclusions

The atmospheric river which made landfall in southwestern B.C. on November 14th, 2021, and the flooding and landslides it caused made this the costliest natural disaster in the province's history. The results presented in this paper characterise the event and its meteorological and hydrological drivers, and evaluate the contribution of human-induced climate change to the event. Drawing together our results, we find that when characterised in terms of storm averaged water vapour transport over the impacted region, the variable typically used to characterise the intensity of atmospheric rivers, the November 2021 AR event was unusual, but not unprecedented. Based on the strength of other westerly events, it was estimated to be about a 1 in 10-year event. When characterised in terms of two-day precipitation it was found to be substantially more extreme, approximately a 1 in 50 to 1 in 100-year event. When characterised in terms of peak streamflow, return periods varied across the region, but exceeded 1 in 100-year events in several basins.

An analysis of the contributions to the extreme streamflow indicated that the very high precipitation during the event was the primary driver, but that snowmelt associated with a rapid rise in temperatures during the event also made a significant contribution over most basins. Relatively wet conditions prior to the event also contributed. While wildfire has been suggested as having contributed to the severity of the impacts in some places, the small fraction of most basins in the region which burnt in recent years, including the Sumas River and Coquihalla River basins, preclude wildfire having been a primary driver of the event's impacts.

An event attribution analysis applied to vapour transport indicated that the probability of a westerly atmospheric river event as strong as that observed has been increased by at least 60% by the effects of human-induced climate change, and a similar analysis applied to two-day precipitation events at least as strong as that observed in 2021 indicated that human influence had increased their likelihood by a best estimate of 45%. Similarly, an event attribution analysis applied to October–December peak streamflow for several basins in the impacted area indicated that 1 in 100-year peak streamflow has been increased by 16–63% by the effects of human-induced climate change, with the probability of a 1 in 100-year event comparable to that observed having increased by a best estimate ranging from 120% to 330% across basins.

Drawing these results together indicates that human-induced climate change contributed substantially to the probability of the November 2021 atmospheric river event and associated flooding. Our results further indicate that the probability of such events is expected to increase further in the future, demonstrating the importance of developing increased resiliency to such events here in B.C., and across the world.

Author statement

Nathan P. Gillett: Conceptualization, Methodology, Writing – Original Draft, Project administration, Supervision.

Alex J. Cannon: Conceptualization, Methodology, Validation, Formal analysis, Investigation, Writing – Original Draft, Visualization.

Elizaveta Malinina: Methodology, Validation, Formal analysis, Investigation, Writing – Review & Editing, Visualization.

Markus Schnorbus: Methodology, Formal analysis, Investigation, Writing – Original Draft, Visualization, Supervision.

Faron Anslow: Formal analysis, Investigation, Writing – Review & Editing, Visualization.

Qiaohong Sun: Validation, Formal analysis, Investigation, Writing – Original Draft, Visualization.

Megan Kirchmeier-Young: Formal analysis, Investigation, Writing – Original Draft, Visualization.

Francis Zwiers: Conceptualization, Methodology, Writing – Review & Editing, Supervision.

Christian Seiler: Formal analysis, Investigation, Visualization.

Xuebin Zhang: Conceptualization, Writing – Review & Editing, Supervision.

Greg Flato: Conceptualization, Supervision.

Hui Wan: Formal analysis.

Guilong Li: Formal analysis.

Armel Castellan: Writing – Review & Editing.

Declaration of competing interest

The authors declare the following financial interests/personal relationships which may be considered as potential competing interests: Francis Zwiers reports financial support was provided by BC Hydro. Xuebin Zhang, a coauthor of this study, is an editor-in-chief at Weather and Climate Extremes.

Acknowledgements

We thank Chun-Chao Kuo and David Campbell at the B.C. River Forecast Centre for providing the streamflow data, including the 2021 event values, and Marc Beauchemin at Environment and Climate

Change Canada for providing CaPA data. We thank the B.C. Ministry of Transportation and Infrastructure for the list of road impacts locations. We thank John Fyfe (ECCC) for providing comments on the manuscript. Support for the VIC-GL hydrological simulations was provided by Compute Canada and BC Hydro.

Appendix A. Supplementary data

Supplementary data to this article can be found online at https://doi.org/10.1016/j.wace.2022.100441.

References

Bell, B., Hersbach, H., Simmons, A., Berrisford, P., Dahlgren, P., Horányi, A., et al., 2021. The ERA5 global reanalysis: preliminary extension to 1950. Q. J. R. Meteorol. Soc. 147 (741), 4186–4227. https://doi.org/10.1002/qj.4174.

Carrol, T., Cline, D., Fall, G., Nilsson, A., Li, L., Rost, A., 2001. NOHRSC operations and the simulations of snow cover properties for the coterminous U.S. In: 69th Annual Meeting of the Western Snow Conference, Sun Valley, Idaho. https://www.nohrsc.noaa.gov/technology/pdf/wsc2001.pdf.

Douville, H., Raghavan, K., Renwick, J., Allan, R.P., Arias, P.A., Barlow, M., Cerezo-Mota, R., Cherchi, A., Gan, T.Y., Gergis, J., Jiang, D., Khan, A., Pokam Mba, W., Rosenfeld, D., Tierney, J., Zolina, O., 2021. Water cycle changes. In: Masson-Delmotte, V., Zhai, P., Pirani, A., Connors, S.L., Péan, C., Berger, S., Caud, N., Chen, Y., Goldfarb, L., Gomis, M.I., Huang, M., Leitzell, K., Lonnoy, E., Matthews, J. B.R., Maycock, T.K., Waterfield, T., Yelekçi, O., Yu, R., Zhou, B. (Eds.), Climate Change 2021: the Physical Science Basis. Contribution of Working Group I to the Sixth Assessment Report of the Intergovernmental Panel on Climate Change. Cambridge University Press, pp. 1055–1210. https://doi.org/10.1017/9781009157896.010.

Ebel, B.A., Martin, D.A., 2017. Meta-analysis of field-saturated hydraulic conductivity recovery following wildland fire: applications for hydrologic model parameterization and resilience assessment. Hydrol. Process. 31, 3682–3696. https://doi.org/10.1002/hyp.11288.

El Adlouni, S., Ouarda, T.B., Zhang, X., Roy, R., Bobée, B., 2007. Generalized maximum likelihood estimators for the nonstationary generalized extreme value model. Water Resour. Res. 43 (3), W03410 https://doi.org/10.1029/2005WR004545.

Eyring, V., Bony, S., Meehl, G.A., Senior, C.A., Stevens, B., Stouffer, R.J., Taylor, K.E., 2016a. Overview of the coupled model intercomparison Project phase 6 (CMIP6) experimental design and organization. Geosci. Model Dev. (GMD) 9 (5), 1937–1958. https://doi.org/10.5194/gmd-9-1937-2016.

Eyring, V., Righi, M., Lauer, A., Evaldsson, M., Wenzel, S., Jones, C., et al., 2016b. ESMValTool (v1.0)–a community diagnostic and performance metrics tool for routine evaluation of Earth system models in CMIP. Geosci. Model Dev. (GMD) 9 (5), 1747–1802. https://doi.org/10.5194/gmd-9-1747-2016.

Eyring, V., Gillett, N.P., Achuta Rao, K.M., Barimalala, R., Barreiro Parrillo, M., Bellouin, N., Cassou, C., Durack, P.J., Kosaka, Y., McGregor, S., Min, S., Morgenstern, O., Sun, Y., 2021. Human influence on the climate system. In: Masson-Delmotte, V., Zhai, P., Pirani, A., Connors, S.L., Péan, C., Berger, S., Caud, N., Chen, Y., Goldfarb, L., Gomis, M.I., Huang, M., Leitzell, K., Lonnoy, E., Matthews, J. B.R., Maycock, T.K., Waterfield, T., Yelekçi, O., Yu, R., Zhou, B. (Eds.), Climate Change 2021: the Physical Science Basis. Contribution of Working Group I to the Sixth Assessment Report of the Intergovernmental Panel on Climate Change. Cambridge University Press, pp. 423–552. https://doi.org/10.1017/9781009157896.005.

Fleming, S.W., Whitfield, P.H., Moore, R.D., Quilty, E.J., 2007. Regime-dependent streamflow sensitivities to Pacific climate modes cross the Georgia–Puget transboundary ecoregion. Hydrol. Process. 21, 3264–3287. https://doi.org/10.1002/hyp.6544.

Fortin, V., Roy, G., Stadnyk, T., Koenig, K., Gasset, N., Mahidjiba, A., 2018. Ten years of science based on the Canadian precipitation analysis: a CaPA system overview and literature review. Atmos.-Ocean 56 (3), 178–196. https://doi.org/10.1080/07055900.2018.1474728.

Freudiger, D., Kohn, I., Stahl, K., Weiler, M., 2014. Large-scale analysis of changing frequencies of rain-on-snow events with flood-generation potential. Hydrol. Earth Syst. Sci. 18, 2695–2709. https://doi.org/10.5194/hess-18-2695-2014.

Fyfe, J.C., Derksen, C., Mudryk, L., Flato, G.M., Santer, B.D., Swart, N.C., Molotch, N.P., Zhang, X., Wan, H., Arora, V.K., Scinocca, J., Jiao, Y., 2017. Large near-term projected snowpack loss over the western United States. Nat. Commun. 8, 14996. https://doi.org/10.1038/ncomms14996.

Gasset, N., Fortin, V., Dimitrijevic, M., Carrera, M., Bilodeau, B., Muncaster, R., et al., 2021. A 10 km North American precipitation and land-surface reanalysis based on the GEM atmospheric model. Hydrol. Earth Syst. Sci. 25 (9), 4917–4945. https://doi.org/10.5194/hess-25-4917-2021.

Guan, B., Waliser, D.E., Ralph, F.M., Fetzer, E.J., Neiman, P.J., 2016. Hydrometeorological characteristics of rain-on-snow events associated with atmospheric rivers. Geophys. Res. Lett. 43, 2964–2973. https://doi.org/10.1002/2016GL067978.

Hersbach, H., Bell, B., Berrisford, P., Hirahara, S., Horányi, A., Muñoz-Sabater, J., et al., 2020. The ERA5 global reanalysis. Q. J. R. Meteorol. Soc. 146 (730), 1999–2049. https://doi.org/10.1002/qj.3803.

Hubbard, L.L., 1994. Floods of November 1990 in Western Washington. U.S. Geological Survey. Open-File Report 93-631. https://pubs.usgs.gov/of/1993/0631/report.pdf.

Insurance Bureau of Canada, 2021. British Columbia floods cause $450 million in insured damage. http://www.ibc.ca/bc/resources/media-centre/media-releases/british-columbia-floods-cause-450-million-in-insured-damage.

IPCC, 2021. Summary for policymakers. In: Masson-Delmotte, V., Zhai, P., Pirani, A., Connors, S.L., Péan, C., Berger, S., Caud, N., Chen, Y., Goldfarb, L., Gomis, M.I., Huang, M., Leitzell, K., Lonnoy, E., Matthews, J.B.R., Maycock, T.K., Waterfield, T., Yelekçi, O., Yu, R., Zhou, B. (Eds.), Climate Change 2021: the Physical Science Basis. Contribution of Working Group I to the Sixth Assessment Report of the Intergovernmental Panel on Climate Change, pp. 3–32. https://doi.org/10.1017/9781009157896.001.

Jordan, P., 2015. Post-wildfire debris flows in southern British Columbia, Canada. Int. J. Wildland Fire 25, 322–336. https://doi.org/10.1071/WF14070.

Kim, J., Waliser, D.E., Neiman, P.J., Guan, B., Ryoo, J.-M., Wick, G.A., 2013. Effects of atmospheric river landfalls on the cold season precipitation in California. Clim. Dynam. 40, 465–474. https://doi.org/10.1007/s00382-012-1322-3.

Kirchmeier-Young, M.C., Gillett, N.P., Zwiers, F.W., Cannon, A.J., Anslow, F.S., 2019. Attribution of the influence of human-induced climate change on an extreme fire season. Earth's Future 7, 2–10. https://doi.org/10.1029/2018EF001050.

Lespinas, F., Fortin, V., Roy, G., Rasmussen, P., Stadnyk, T., 2015. Performance evaluation of the Canadian precipitation analysis (CaPA). J. Hydrometeorol. 16 (5), 2045–2064. https://doi.org/10.1175/JHM-D-14-0191.1.

Li, D., Lettenmaier, D.P., Margulis, S.A., Andreadis, K., 2019. The role of rain-on-snow in flooding over the conterminous United States. Water Resour. Res. 55, 8492–8513. https://doi.org/10.1029/2019WR024950.

Martins, E.S., Stedinger, J.R., 2000. Generalized maximum-likelihood generalized extreme-value quantile estimators for hydrologic data. Water Resour. Res. 36 (3), 737–744. https://doi.org/10.1029/1999WR900330.

McCabe, G.J., Clark, M.P., Hay, L.E., 2007. Rain-on-snow events in the western United States. Bull. Am. Meteorol. Soc. 88, 319–328. https://doi.org/10.1175/BAMS-88-3-319.

Merz, R., Blöschl, G., 2003. A process typology of regional floods. Water Resour. Res. 39 https://doi.org/10.1029/2002WR001952.

Ministry of Environment and Climate Change Strategy, 2009. Automated Snow Weather Stations - Province of British Columbia. https://www2.gov.bc.ca/gov/content/environment/air-land-water/water/water-science-data/water-data-tools/snow-survey-data/automated-snow-weather-stations. (Accessed 19 January 2022).

Mo, R., So, R., Brugman, M.M., Mooney, C., Liu, A.Q., Jakob, M., et al., 2021. Column relative humidity and primary condensation rate as two useful supplements to atmospheric river analysis. Water Resour. Res. 57 (11), e2021WR029678 https://doi.org/10.1029/2021WR029678.

Müller, W.A., Jungclaus, J.H., Mauritsen, T., Baehr, J., Bittner, M., Budich, R., et al., 2018. A higher-resolution version of the Max Planck institute earth system model (MPI-ESM1. 2-HR). J. Adv. Model. Earth Syst. 10 (7), 1383–1413. https://doi.org/10.1029/2017MS001217.

Mundhenk, B.D., Barnes, E.A., Maloney, E.D., Nardi, K.M., 2016. Modulation of atmospheric rivers near Alaska and the U.S. West Coast by northeast Pacific height anomalies. J. Geophys. Res. 121 (21), 12,751–12,765. https://doi.org/10.1002/2016JD025350.

Musselman, K.N., Lehner, F., Ikeda, K., Clark, M.P., Prein, A.F., Liu, C., Barlage, M., Rasmussen, R., 2018. Projected increases and shifts in rain-on-snow flood risk over western North America. Nat. Clim. Change 8, 808–812. https://doi.org/10.1038/s41558-018-0236-4.

National Operational Hydrologic Remote Sensing Center, 2004. Snow Data Assimilation System (SNODAS) Data Products at NSIDC, Version 1. NSIDC: National Snow and Ice Data Center, Boulder, Colorado USA. https://doi.org/10.7265/N5TB14TC. (Accessed 30 December 2021).

Natural Resources Conservation Service, 2022. Automated Snow Monitoring. Monitoring Programs. https://www.nrcs.usda.gov/wps/portal/wcc/home/aboutUs/monitoringPrograms/automatedSnowMonitoring/. (Accessed 19 January 2022).

Neiman, P.J., Ralph, F.M., Wick, G.A., Lundquist, J.D., Dettinger, M.D., 2008. Meteorological characteristics and overland precipitation impacts of atmospheric rivers affecting the west coast of North America based on eight years of SSM/I satellite observations. J. Hydrometeorol. 9, 22–47. https://doi.org/10.1175/2007JHM855.1.

Neiman, P.J., Schick, L.J., Ralph, F.M., Hughes, M., Wick, G.A., 2011. Flooding in western Washington: the connection to atmospheric rivers. J. Hydrometeorol. 12, 1337–1358. https://doi.org/10.1175/2011JHM1358.1.

Ohba, M., Kawase, H., 2020. Rain-on-Snow events in Japan as projected by a large ensemble of regional climate simulations. Clim. Dynam. 55, 2785–2800. https://doi.org/10.1007/s00382-020-05419-8.

O'Neill, B.C., Tebaldi, C., van Vuuren, D.P., Eyring, V., Friedlingstein, P., Hurtt, G., et al., 2016. The scenario model intercomparison Project (ScenarioMIP) for CMIP6. Geosci. Model Dev. (GMD) 9, 3461–3482. https://doi.org/10.5194/gmd-9-3461-2016.

Parise, M., Cannon, S.H., 2012. Wildfire impacts on the processes that generate debris flows in burned watersheds. Nat. Hazards 61, 217–227. https://doi.org/10.1007/s11069-011-9769-9.

R Core Team, 2019. R: A Language and Environment for Statistical Computing. R Foundation for Statistical Computing, Vienna, Austria. https://www.r-project.org/.

Ralph, F.M., Coleman, T., Neiman, P.J., Zamora, R.J., et al., 2013. Observed impacts of duration and seasonality of atmospheric-river landfalls on soil moisture and runoff in coastal northern California. J. Hydrometeorol. 14 (2), 443–459. https://doi.org/10.1175/JHM-D-12-076.1.

Ralph, F.M., Dettinger, M.D., Cairns, M.M., Galarneau, T.J., et al., 2018. Defining "atmospheric river": how the Glossary of Meteorology helped resolve a debate. Bull. Am. Meteorol. Soc. 99 (4), 837–839. https://doi.org/10.1175/BAMS-D-17-0157.1.

Ralph, F.M., Rutz, J.J., Cordeira, J.M., Dettinger, M., Anderson, M., Reynolds, D., et al., 2019. A scale to characterize the strength and impacts of atmospheric rivers. Bull. Am. Meteorol. Soc. 100 (2), 269–289. https://doi.org/10.1175/BAMS-D-18-0023.1.

Rivoire, P., Martius, O., Naveau, P., 2021. A comparison of moderate and extreme ERA-5 daily precipitation with two observational data sets. Earth Space Sci. 8 (4), e2020EA001633 https://doi.org/10.1029/2020EA001633.

Rodgers, K.B., Lee, S.S., Rosenbloom, N., Timmermann, A., Danabasoglu, G., Deser, C., et al., 2021. Ubiquity of human-induced changes in climate variability. Earth Syst. Dynam. 12 (4), 1393–1411. https://doi.org/10.5194/esd-12-1393-2021.

Schnorbus, M., 2018. VIC glacier: description of VIC model changes and updates (PCIC internal report). Pacific Climate Impacts Consortium, 1–39. Victoria, BC.

Scinocca, J.F., Kharin, V.V., Jiao, Y., Qian, M.W., Lazare, M., Solheim, L., Flato, G.M., Biner, S., Desgagne, M., Dugas, B., 2016. Coordinated global and regional climate modeling. J. Clim. 29, 17–35. https://doi.org/10.1175/JCLI-D-15-0161.1.

Seneviratne, S.I., Zhang, X., et al., 2021. Weather and climate extreme events in a changing climate. In: Masson-Delmotte, V., Zhai, P., Pirani, A., Connors, S.L., Péan, C., Berger, S., Caud, N., Chen, Y., Goldfarb, L., Gomis, M.I., Huang, M., Leitzell, K., Lonnoy, E., Matthews, J.B.R., Maycock, T.K., Waterfield, T., Yelekçi, O., Yu, R., Zhou, B. (Eds.), Climate Change 2021: the Physical Science Basis. Contribution of Working Group I to the Sixth Assessment Report of the Intergovernmental Panel on Climate Change. Cambridge University Press, pp. 1513–1766. https://doi.org/10.1017/9781009157896.013.

Sharma, A.R., Déry, S.J., 2020a. Contribution of atmospheric rivers to annual, seasonal, and extreme precipitation across British Columbia and southeastern Alaska. J. Geophys. Res. Atmos. 125 (9), e2019JD031823 https://doi.org/10.1029/2019JD031823.

Sharma, A.R., Déry, S.J., 2020b. Linking atmospheric rivers to annual and extreme river runoff in British Columbia and southeastern Alaska. J. Hydrometeorol. 21 (11), 2457–2472. https://doi.org/10.1175/JHM-D-19-0281.1.

Sharma, A.R., Déry, S.J., 2020c. Variability and trends of landfalling atmospheric rivers along the Pacific Coast of northwestern North America. Int. J. Climatol. 40 (1), 544–558. https://doi.org/10.1002/joc.6227.

Shu, J., Shamseldin, A.Y., Weller, E., 2021. The impact of atmospheric rivers on rainfall in New Zealand. Sci. Rep. 11 https://doi.org/10.1038/s41598-021-85297-0.

Sun, Q., Zhang, X., Zwiers, F., Westra, S., Alexander, L.V., 2021. A global, continental, and regional analysis of changes in extreme precipitation. J. Clim. 34 (1), 243–258. https://doi.org/10.1175/JCLI-D-19-0892.1.

Trubilowicz, J.W., Moore, R.D., 2017. Quantifying the role of the snowpack in generating water available for run-off during rain-on-snow events from snow pillow records. Hydrol. Process. 31, 4136–4150. https://doi.org/10.1002/hyp.11310.

Warner, M.D., Mass, C.F., Salathé Jr., E.P., 2012. Wintertime extreme precipitation events along the Pacific Northwest coast: climatology and synoptic evolution. Mon. Weather Rev. 140 (7), 2021–2043. https://doi.org/10.1175/MWR-D-11-00197.1.

Wasko, C., Nathan, R., 2019. Influence of changes in rainfall and soil moisture on trends in flooding. J. Hydrol. 575, 432–441. https://doi.org/10.1016/j.jhydrol.2019.05.054.

Wasko, C., Nathan, R., Peel, M.C., 2020. Changes in antecedent soil moisture modulate flood seasonality in a changing climate. Water Resour. Res. 56, e2019WR026300 https://doi.org/10.1029/2019WR026300.

Werner, A.T., Cannon, A.J., 2016. Hydrologic extremes–an intercomparison of multiple gridded statistical downscaling methods. Hydrol. Earth Syst. Sci. 20 (4), 1483–1508. https://doi.org/10.5194/hess-20-1483-2016.

Werner, A.T., Schnorbus, M.A., Shrestha, R.R., et al., 2019. A long-term, temporally consistent, gridded daily meteorological dataset for northwestern North America. Sci. Data 6, 180299. https://doi.org/10.1038/sdata.2018.299.

Whan, K., Zwiers, F., 2016. Evaluation of extreme rainfall and temperature over North America in CanRCM4 and CRCM5. Clim. Dynam. 46 (11), 3821–3843. https://doi.org/10.1007/s00382-015-2807-7.

Whitfield, P.H., Cannon, A.J., Reynolds, C.J., 2002. Modelling streamflow in present and future climates: examples from the Georgia Basin, British Columbia. Can. Water Resour. J. 27, 427–456. https://doi.org/10.4296/cwrj2704427.

Winkler, R.D., Moore, R.D., Redding, T.E., Spittlehouse, D.L., Smerdon, B.D., Carlyle-Moses, D.E., 2010. The effects of forest disturbance on hydrologic processes and watershed response. In: Pike, R.G., Redding, T.E., Moore, R.D., Winkler, R.D., Bladon, K.D. (Eds.), Compendium of Forest Hydrology and Geomorphology in British Columbia. B.C. Min. For. Range, Victoria, B.C., and FORREX, pp. 179–212. Land Manag. Handb. 66. https://www.for.gov.bc.ca/hfd/pubs/docs/lmh/Lmh66/Lmh66_ch07.pdf.

Würzer, S., Jonas, T., Wever, N., Lehning, M., 2016. Influence of initial snowpack properties on runoff formation during rain-on-snow events. J. Hydrometeorol. 17, 1801–1815. https://doi.org/10.1175/JHM-D-15-0181.1.

Yukimoto, S., Kawai, H., Koshiro, T., Oshima, N., Yoshida, K., Urakawa, S., et al., 2019. The Meteorological Research Institute Earth System Model Version 2.0, MRI-ESM2.0: Description and basic evaluation of the physical component. J. Meteorol. Soc. Jpn. 97, 931–965. https://doi.org/10.2151/jmsj.2019-051.